Teleseismic inversion for rupture process of the 27 February 2010 Chile (M$_w$ 8.8) earthquake

T. Lay,[1] C. J. Ammon,[2] H. Kanamori,[3] K. D. Koper,[4] O. Sufri,[4] and A. R. Hutko[5]

[1] The 27 February 2010 Chile (M$_w$ 8.8) earthquake is the fifth largest earthquake to strike during the age of seismological instrumentation. The faulting geometry, slip distribution, seismic moment, and moment-rate function are estimated from broadband teleseismic P, SH, and Rayleigh wave signals. We explore some of the trade-offs in the rupture-process estimation due to model parameterizations, limited teleseismic sampling of seismic phase velocities, and uncertainty in fault geometry. The average slip over the ~81,500 km^2 rupture area is about 5 m, with slip concentrations down-dip, up-dip and southwest, and up-dip and north of the hypocenter. Relatively little slip occurred up-dip/offshore of the hypocenter. The average rupture velocity is ~2.0–2.5 km/s. **Citation:** Lay, T., C. J. Ammon, H. Kanamori, K. D. Koper, O. Sufri, and A. R. Hutko (2010), Teleseismic inversion for rupture process of the 27 February 2010 Chile (M$_w$ 8.8) earthquake, *Geophys. Res. Lett.*, *37*, L13301, doi:10.1029/2010GL043379.

1. Introduction

[2] On 27 February 2010, central Chile experienced a great earthquake (06:34:14 UTC, epicenter 35.909°S, 72.733°W, 35 km depth (U.S. Geological Survey, Magnitude 8.8—Offshore Maule, Chile, 2010, http://earthquake.usgs.gov/earthquakes/eqinthenews/2010/us2010tfan/) that ruptured about 550 km along the megathrust bounding the subducting Nazca plate and the overriding South American plate. The aftershock distribution (Figure 1 and Animation S1 of the auxiliary material) indicates that the event filled a seismic gap along the 1835 earthquake rupture zone, and that the rupture also extended well to the north, spanning regions that ruptured in 1928, 1985 and about 2/3 of the 1906 rupture zone [*Beck et al.*, 1998].[6] The 1835 gap had been the subject of recent seismic and geodetic investigations [*Haberland et al.*, 2009; *Ruegg et al.*, 2009], which provide constraints on the megathrust geometry and the down-dip extent of the previously locked region. Aftershocks also extend southward into the northern portion the 1960 rupture zone, where recent seismic studies have also

been conducted to constrain the megathrust geometry [*Groß et al.*, 2008].

[3] The Global Centroid Moment Tensor (GCMT) solution for the great 2010 Chile event has a seismic moment M$_o$ = 1.84 × 10^{22} Nm (M$_w$ 8.8), a centroid location of 35.95°S, 73.15°W, and a best double couple fault plane geometry of strike $\varphi = 18°$ and dip $\delta = 18°$ with a rake $\lambda = 112°$ (G. Ekström, Global CMT Web Site, 2010, http://www.globalcmt.org/). W-phase inversion [*Kanamori and Rivera*, 2008] using 46 stations and 72 channels of long-period ground motions in the 0.001–0.005 Hz passband yields a solution with M$_o$ = 2.0 × 10^{22} Nm with centroid location of 35.95°S, 72.75°W, a centroid time of 61.4 s, and a best-fitting fault plane having $\varphi = 18°$ and $\delta = 16°$ with $\lambda = 109°$. W-phase inversions using lower frequency passbands yield similar solutions with no strong increase in M$_o$, which together with the lack of non-double couple components in the above point-source solutions suggests that there is no major complexity in the fault geometry.

2. Teleseismic Wave Constraints

[4] Finite-fault rupture models represent the space-time distribution of slip (or seismic moment) on a parameterized fault surface. Differential times and amplitudes of seismic waves arriving at stations distributed around the source provide the resolution of slip history. Inversions of teleseismic body waves typically use data in the epicentral distance range 30–100°, for which propagation effects are minimal, but wave apparent velocities are high. Even for a great rupture like the 2010 event, the subevents within the rupture produce differential times of up to only a few seconds for teleseismic P and S waves. As a result, parameterization of the rupture process can strongly influence the slip model estimates, with rupture velocity and subfault rupture duration having first-order influence [e.g., *Lay et al.*, 2010]. This is well-known, but many differences between slip models that are debated stem directly from model assumptions, data distribution, and intrinsic range of apparent velocities contained within the observations. Initial inversions of teleseismic P and SH observations with excellent azimuthal distribution indicated strong trade-offs in assumed rupture velocity and bilateral slip extent (the spatial pattern of time-integrated slip effectively stretches proportionally to the rupture velocity), so it is important to independently estimate rupture velocity.

[5] There are two viable approaches to better constraining the rupture velocity from teleseismic observations; use of broadband surface waves, which have a range of apparent velocities close to that of most rupture speeds, enhancing

[1]Department of Earth and Planetary Sciences, University of California, Santa Cruz, California, USA.
[2]Department of Geosciences, Pennsylvania State University, University Park, Pennsylvania, USA.
[3]Seismological Laboratory, California Institute of Technology, Pasadena, California, USA.
[4]Department of Earth and Atmospheric Sciences, Saint Louis University, Saint Louis, Missouri, USA.
[5]Data Management Center, Incorporated Research Institutions for Seismology, Seattle, Washington, USA.
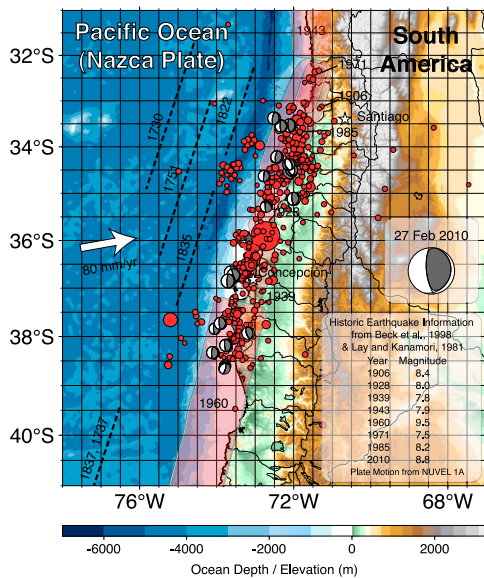
[6]Auxiliary materials are available in the HTML. doi:10.1029/2010GL043379.

Figure 1. Map of the source region of the 2010 Chile earthquake. The large red circle is the mainshock epicenter (http://earthquake.usgs.gov/earthquakes/eqinthenews/2010/us2010tfan/), and other red dots are aftershocks with radius scaled proportional to seismic magnitude at the USGS locations. The gray focal mechanisms are GCMT (http://www.globalcmt.org/) solutions for larger aftershocks at their centroid locations. The approximate rupture extents of previous large earthquakes in the region are shown in pink or indicated by the offshore dashed curves, with the seismic magnitudes given in the inset. The 1939 event near Concepción was an intra-slab rupture, but the others are believed to have been on the megathrust.

their sensitivity to finite-source directivity [e.g., *Ammon et al.*, 2006], and using seismic networks to image short-period radiation by back-projection methods [e.g., *Ishii et al.*, 2005; *Xu et al.*, 2009]. We use both approaches here.

[6] Back-projecting P wave data from large networks of stations spanning a limited azimuthal range (such that the variation in Green's functions to the stations is minor) can directly image coherent high-frequency radiation from the rupture. For the Chile event, North America has a large concentration of stations with coherent waveforms close to the strike direction (see Figure S1) that provide good resolution of northward rupture propagation. Variable radiation pattern or directivity effects of southward propagation may obscure energy release from the slip front propagating away from the network. Figure 2 shows several time slices of a continuous back-projection (see the full animation in Animation S2) of P waves from 49 North American stations filtered in the 0.2–2.0 Hz passband. Beams were constructed with 4th root stacking in time steps of 1 sec for a grid of equally spaced points (0.1° by 0.1°) at the nominal hypocentral depth of 35 km. The images indicate an early down-dip, then bi-lateral along-strike rupture propagation in the first 40 s of rupture followed by about 80 s of strong northward rupture propagation for which we estimate an average rupture velocity of about 2.5 km/s. We explored other network configurations, but North America provides the best constraints on overall short-period energy release

pattern (Figure S2). Our results are consistent with those from other groups using similar approaches (e.g., E. Kiser, Preliminary rupture modeling of the February 27, 2010 Chilean earthquake using the Hi-net and USArray Transportable Arrays, 2010, http://seismology.harvard.edu/; GFZ, How the rupture propagated, 2010, http://www.gfz-potsdam.de/portal/gfz/Neuestes/Archive+-+Aus+den+Abteilungen/2010/100304_Teaser-Bruchverlauf-Chileerdbeben2010).

[7] Global broadband short-arc Rayleigh waves (R1) were processed by removing geometrical excitation and propagation effects using the GCMT point-source solution and aspherical phase velocities relative to PREM [see *Ammon et al.*, 2006; *Lay et al.*, 2010]. The resulting R1 source-time functions (STFs) (Figure S3) can be processed for parametric directivity effects (Figure S4) or included directly in finite-fault inversions. The R1 STFs, which contain reliable information in the passband from about 200 s to 70 s, indicate optimal rupture velocities of about 2.25 km/s, with acceptable solutions for values from 2.0–2.5 km/s.

[8] With *a priori* bounds on overall rupture velocity in the range 2.0–2.5 km/s, the inversion of teleseismic P and SH signals becomes much better posed. We inverted 150 s long windows of 29 P waves and 15 SH waves with good azimuthal distribution to determine finite fault slip models for slip-pulse type rupture models with prescribed maximum rupture velocities. A solution is shown in Figure 3a for a
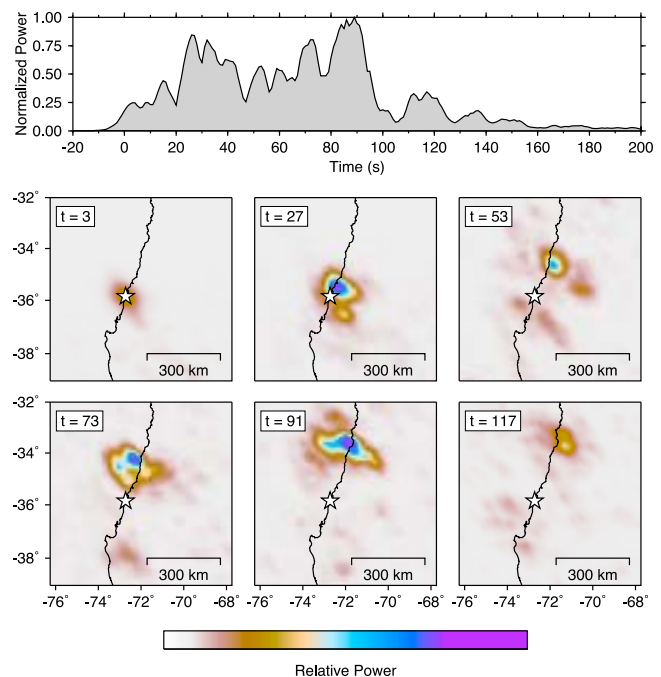

Figure 2. Frames from the animation of P wave back-projection using North American observations from 49 stations filtered in the 0.2–2.0 Hz passband (Animation S2). The signals have been stacked on a grid around the source regions with no *a priori* assumptions about rupture velocity. The color scale indicates relative amplitude from a tapered, 10-s segment of the 4th root beam calculated for each grid point. The times correspond to the midpoint of the sliding window, which is shifted in steps of 1 s. The upper panel shows the maximum beam amplitude on the spatial grid as a function of time.
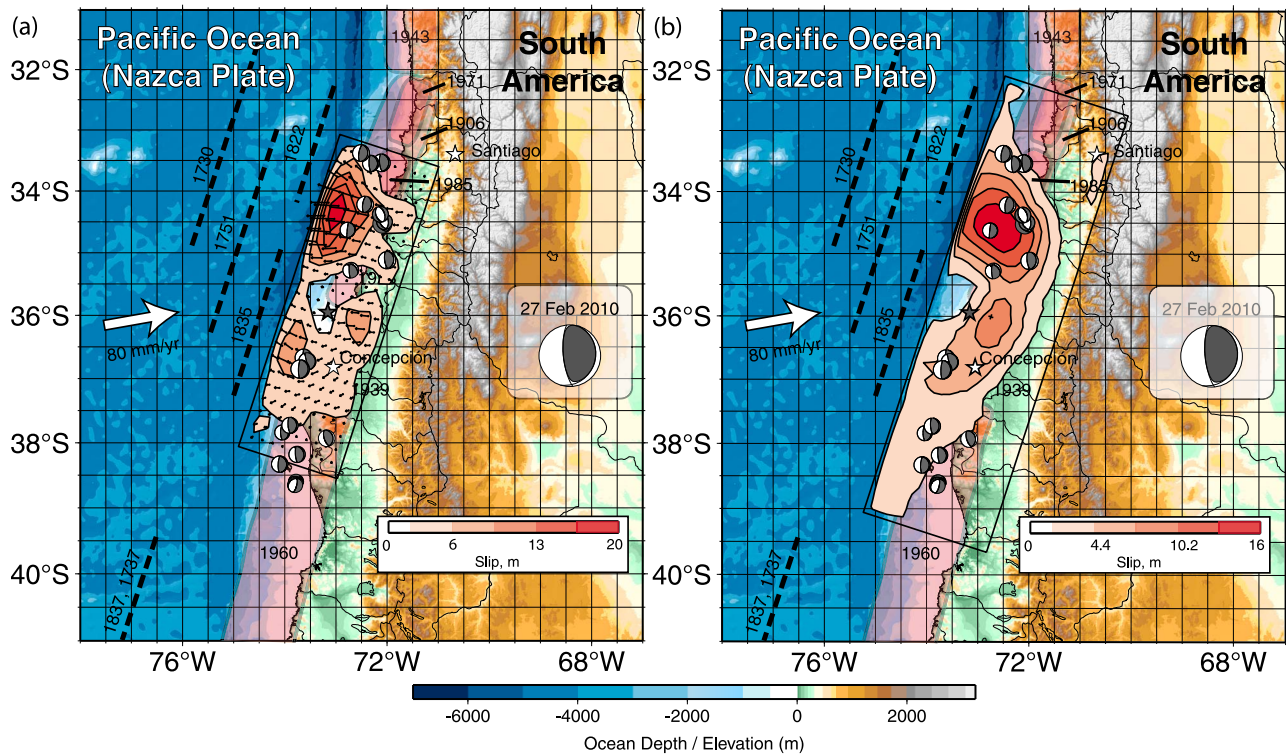
Figure 3. Maps of the finite-fault slip distributions obtained by inversion of (a) teleseismic P and SH waves and (b) teleseismic P waves, SH waves, and R1 STFs. The background map is the same as Figure 1, with the GCMT focal mechanism shown in the insets. The P and SH inversion allows for variable rake at each grid position, with the slip vectors for the hanging wall being shown, and their relative amplitudes contoured. The rupture velocity used for the P and SH inversion was 2.5 km/s and it was 2.25 km/s for the P, SH and R1 STF inversion.

rupture velocity of 2.5 km/s using the fault plane from the GCMT solution ($\varphi = 18°$, $\delta = 18°$) with subfaults having 20 km width down-dip and 25 km length along strike and source time-functions parameterized by 5 overlapping 2.5 s rise-time triangles (total maximum subfault rupture durations of 15 s) with variable strength. This model provides a centroid time of 66 s for the source, and $M_o = 2.6 \times 10^{22}$ Nm, with 89% of the waveform power being accounted for

(Figure S5). The source velocity model was adapted from *Haberland et al.* [2009].

[9] The moment rate function extends for about 130 s (Figure 4), with rather steady increase for 90 s and then an abrupt drop over the last 40 s. The rupture extends bilaterally with an irregular slip distribution that initially is concentrated down-dip from the 35 km deep hypocenter, then spread bilaterally up-dip and off-shore, with two strong slip
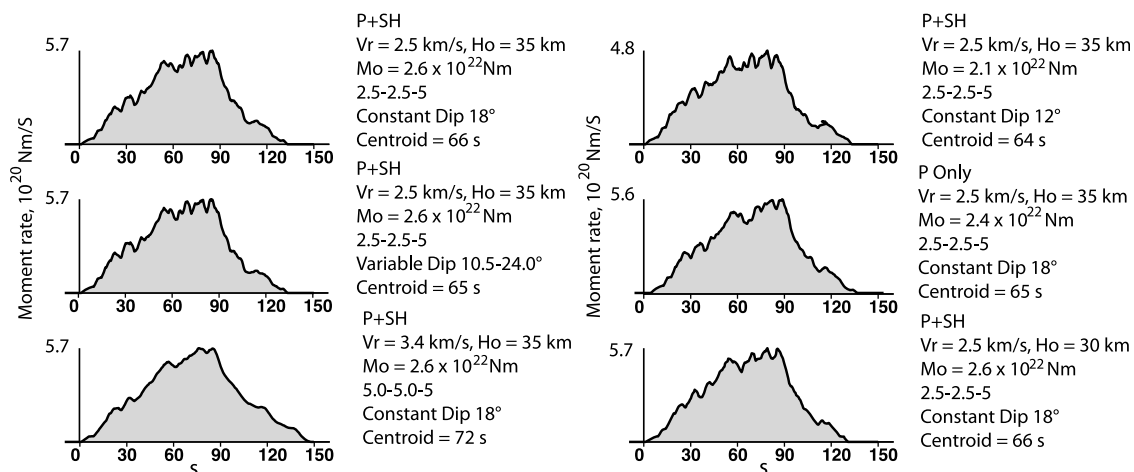

Figure 4. Demonstration of the stability of the moment rate function obtained from teleseismic observations. The results are shown for varying choice of data sets, fault orientation, subfault source-time function (2.5–2.5–5 denotes 5 2.5-s rise-time triangles shifted by 2.5 s), and hypocentral depth (Ho). The centroid time is relatively stable, but does increase if the subfault durations are increased, as does the seismic moment (M_o).

patches in the south and north. The northern patch is substantially stronger in this model, and the basic pattern is a slip-pulse expansion (animations of the cumulative slip and moment rate rupture patterns are in Animations S3 and S4) motivated by the unconstrained back-projections. The concentration of slip in the north is up-dip of the 1985 rupture zone, likely involving release of strain that persisted after that rupture, while aftershock activity appears to have re-ruptured areas within the 1985 segment as well as activating upper plate normal faulting above that rupture zone (Figure 1). The concentration of slip to the north of the epicenter in this model is consistent with several preliminary models based on teleseismic signals (Earthquake Research Institute, Central Chilean earthquake, 2010, http://outreach.eri.u-tokyo.ac.jp/2010/03/201003_centralchile/; G. Hayes, Finite fault model: Preliminary result of the Feb 27, 2010 M_w 8.8 Maule, Chile earthquake, 2010, http://earthquake.usgs.gov/earthquakes/eqinthenews/2010/us2010tfan/finite_fault.php; A. Sladen, Preliminary result 02/27/2010/(Mw 8.8), Chile, 2010, http://www.tectonics.caltech.edu/slip_history/2010_chile/index.html; Y. Yamanaka, 2010, http://www.seis.nagoya-u.ac.jp/sanchu/Seismo_Note/2010/NGY25.html). A solution by G. Shao et al. (Preliminary slip model of the Feb 27, 2010 Mw 8.7 Maule, Chile earthquake, 2010, http://www.geol.ucsb.edu/faculty/ji/big_earthquakes/2010/02/27/chile_2_27.html) places more slip in the southern patch, as does a preliminary joint inversion with a few GPS observations (A. Sladen and S. Owen, Preliminary model combining teleseismic and GPS data 02/27/2010 (Mw 8.8), Chile, 2010, http://www.tectonics.caltech.edu/slip_history/2010_chile/prelim-gps.html). The body wave inversion predicts significant northward amplitude directivity (factor of 2.5 at ~70 s period) for surface waves and matches the primary attributes of the R1 STF signals (Figure S6).

[10] Simultaneous inversion of a data-importance balanced data set with 10 P, 9 SH, and 15 R1 STF signals produced the finite-fault model shown in Figure 3b. We show the solution for a rupture velocity of 2.25 km/s, as that provides the best fit for the R1 signals (Figures S7–S9). The GCMT fault geometry ($\varphi = 18°$, $\delta = 18°$, $\lambda = 112°$) was assumed, and the 15×15 km^2 subfault time functions were restricted to one variable-width half cosine shape with duration limited to range between 16 to 32 s, sufficient to fit the long period signals with a simple subfault parameterization. The Earth model was a one-km deep water layer above a half-space with a P-wave velocity of 6.0 km/s. 87% of the signal power is explained by the model. The estimated $M_o = 2.1 \times 10^{22}$ Nm and the peak slip is about 16 m. The slip centroid is about 54 km north of the hypocenter, and about 24 km up-dip. The basic slip pattern is similar to the body wave solution (Figure 3a), although the slip distribution is slightly contracted due to the lower rupture velocity. The point-source deconvolution reduces depth resolution in the R1 signals, and the centroid of the northern slip patch is slightly deeper than that obtained from the body waves. We consider both models in Figure 3 equally viable given the intrinsic uncertainties and now address the basic question of what aspects of such models are actually resolved.

3. Trade-Offs and Resolution

[11] Finite-fault models involve many assumptions and intrinsic data resolution constraints that make it difficult to

rigorously evaluate confidence in the models. Some parameters, such as planar fault dip can be explored by stepping through many values to at least establish sensitivity. Seldom does a measure of waveform variance reduction provide unambiguous choice of an optimal model. Nonetheless, stability of basic slip patterns can be evaluated. For the P and SH inversions, we explored fault dips ranging from 10° to 20°, given that fits to background seismicity indicate average values of 12° (G. Hayes, Preliminary SZGC results near coast of central Chile, 2010, http://earthquake.usgs.gov/earthquakes/eqarchives/subduction_zone/us2010tfan/index.php), while dips of 14–18° are consistent with regional tomography and geodetic modeling [Haberland et al., 2009; Ruegg et al., 2009] and the long-period point-source inversions give 16–18°. As the fault dip decreases the slip in the southern patch tends to increase relative to the northern patch by 20–30% at up-dip locations, while down-dip slip in the north also increases (Figure S10). We performed inversions with depth varying dip, spanning dips of 10.5 to 24° from shallow subfaults to deep subfaults, finding small changes in the pattern seen in Figure 3a, and no improvement in the overall fit to the signals. For long-period signals from thrust events, the main effect of uncertainty in dip is its trade-off with seismic moment, as the moment estimate scales inversely with dip by a factor of $\sin(2\delta)$ [Kanamori and Given, 1981]. For our body wave inversions, the moment estimates have more complex variation with dip, but experience has shown that moment estimates from body wave finite-fault inversions are not as reliable as those made at long periods due to assumptions used in constructing the Green's functions and unstable resolution of long-period baselines in instrument correction and in the inversion process. Thus, we have more confidence in the R1 STF, W-phase and GCMT solutions for estimates of the ~200 s period seismic moment for the associated dip values. For the GCMT moment we estimate an average slip of 5 m for the 81,500 km^2 region of the fault plane with subfaults having moments at least 10% of the peak subfault moment. The estimated static stress drop over these portions of the fault is 2.3 MPa.

[12] The degree to which the fault rupture is parameterized as a slip-pulse rupture versus a crack-like model can have a major effect on the space-time slip model that is inferred [e.g., Lay et al., 2010]. The excellent fit to the data found assuming an end-member slip-pulse (relatively short subfault durations) behavior indicates that such a model is viable, but comparable fits are obtained if we allow for longer subfault rupture durations (effectively making a wide slip-annulus type model). The moment rate function remains quite stable for such models (Figure 4), as are the slip functions (Figure S11). Rupture kinematics are also influenced by choice of hypocentral depth, which we varied from 20 to 40 km, but the overall slip pattern was not strongly affected.

4. Discussion

[13] Teleseismic P, SH, and Rayleigh waves have been used to construct finite-fault models describing the space-time history of faulting for the 27 February 2010 great Chile earthquake. These models have some stable attributes and some clear uncertainties associated with imperfect knowledge of the fault geometry, the fundamental nature of the

faulting process and the near-source velocity structure. Rupture velocity is bounded to 2.0–2.5 km/s using array back-projection methods and broadband surface waves. Slip-pulse type models with these velocities achieve excellent matches to teleseismic observations. The slip models found for a wide range of assumed geometries and subfault parameters tend to share concentrations of slip down-dip of the hypocenter, up-dip toward the southwest and up-dip toward the north. The basic features of our models provide a first-order characterization of the great 2010 Chile earthquake rupture.

References

Ammon, C. J., A. A. Velasco, and T. Lay (2006), Rapid estimation of first-order rupture characteristics for large earthquakes using surface waves: 2004 Sumatra-Andaman earthquake, *Geophys. Res. Lett.*, *33*, L14314, doi:10.1029/2006GL026303.

Beck, S., S. Barientos, E. Kausel, and M. Reyes (1998), Source characteristics of historic earthquake along the central Chile subduction zone, *J. South Am. Earth Sci.*, *11*, 115–129, doi:10.1016/S0895-9811(98)00005-4.

Groß, K., U. Miksch, and TIPTEQ Research Group Seismics Team (2008), The reflection seismic survey of project TIPTEQ—The inventory of the Chilean subduction zone at 38.2°S, *Geophys. J. Int.*, *172*, 565–571, doi:10.1111/j.1365-246X.2007.03680.x.

Haberland, C., A. Rietbrock, D. Lange, K. Bataille, and T. Dahm (2009), Structure of the seismogenic zone of the southcentral Chilean margin revealed by local earthquake traveltime tomography, *J. Geophys. Res.*, *114*, B01317, doi:10.1029/2008JB005802.

Ishii, M., P. M. Shearer, H. Houston, and J. E. Vidale (2005), Extent, duration and speed of the 2004 Sumatra-Andaman earthquake imaged by the Hi-net array, *Nature*, *435*, 933–936.

Kanamori, H., and J. W. Given (1981), Use of long-period surface waves for rapid determination of earthquake source parameters, *Phys. Earth Planet. Inter.*, *27*, 8–31, doi:10.1016/0031-9201(81)90083-2.

Kanamori, H., and L. Rivera (2008), Source inversion of *W*-phase: Speeding up seismic tsunami warning, *Geophys. J. Int.*, *175*, 222–238, doi:10.1111/j.1365-246X.2008.03887.x.

Lay, T., and H. Kanamori (1981), An asperity model of large earthquake sequences, in *Earthquake Prediction: An International Review, Maurice Ewing Ser*, vol. 4, edited by D. W. Simpson and P. G. Richards, pp. 579–592, AGU, Washington, D. C.

Lay, T., C. J. Ammon, A. R. Hutko, and H. Kanamori (2010), Effects of kinematic constraints on teleseismic finite-source rupture inversions: Great Peruvian earthquakes of 23 June 2001 and 15 August 2007, *Bull. Seismol. Soc. Am.*, *100*, 969–994, doi:10.1785/0120090274.

Ruegg, J. C., A. Rudloff, C. Vigny, R. Madariaga, J. B. de Chabalier, J. Campos, E. Kausel, S. Barrientos, and D. Dimitrov (2009), Interseismic strain accumulation measured by GPS in the seismic gap between Constitución and Concepción in Chile, *Phys. Earth Planet. Inter.*, *175*, 78–85, doi:10.1016/j.pepi.2008.02.015.

Xu, Y., K. D. Koper, O. Sufri, L. Zhu, and A. R. Hutko (2009), Rupture imaging of the M_w 7.9 12 May 2008 Wenchuan earthquake from back projection of teleseismic P waves, *Geochem. Geophys. Geosyst.*, *10*, Q04006, doi:10.1029/2008GC002335.

C. J. Ammon, Department of Geosciences, Pennsylvania State University, 440 Deike Bldg., University Park, PA 16802, USA.

A. R. Hutko, Data Management Center, Incorporated Research Institutions for Seismology, 1408 NE 45 St., Ste. 201, Seattle, WA 98105, USA.

H. Kanamori, Seismological Laboratory, California Institute of Technology, 1200 East California Blvd., Pasadena, CA 91125, USA.

K. D. Koper and O. Sufri, Department of Earth and Atmospheric Sciences, Saint Louis University, 3642 Lindell Blvd., Saint Louis, MO 63108, USA.

T. Lay, Department of Earth and Planetary Sciences, University of California, 1156 High St., Santa Cruz, CA 95064, USA. (thorne@pmc.ucsc.edu)